Aerosol Direct Writing and Thermal Tuning of Copper Nanoparticle Patterns as Surface-Enhanced Raman Scattering Sensors

Aghajani, Saleh; Accardo, Angelo; Tichem, Marcel

DOI
10.1021/acsanm.0c00887

Publication date
2020

Document Version
Final published version

Published in
ACS Applied Nano Materials

Citation (APA)
Aghajani, S., Accardo, A., & Tichem, M. (2020). Aerosol Direct Writing and Thermal Tuning of Copper Nanoparticle Patterns as Surface-Enhanced Raman Scattering Sensors. *ACS Applied Nano Materials*, *3*(6), 5665-5675. https://doi.org/10.1021/acsanm.0c00887

ACS APPLIED NANO MATERIALS

www.acsanm.org

Article

Aerosol Direct Writing and Thermal Tuning of Copper Nanoparticle Patterns as Surface-Enhanced Raman Scattering Sensors

Saleh Aghajani,* Angelo Accardo, and Marcel Tichem

Cite This: *ACS Appl. Nano Mater.* 2020, 3, 5665−5675

ABSTRACT: Surface-enhanced Raman scattering (SERS) substrates are of great interest for detecting low-concentrated analytes. However, issues such as multistep processing, cost, and possible presence of hazardous substances in the fabrication still represent a significant drawback. In this paper, an innovative direct writing method is introduced for solvent-free and spatially selective deposition of fine metal copper nanoparticles (CuNPs), with size distribution below 20 nm, generated in-line through a spark ablation method (SAM). The deposited CuNPs' morphology and composition were characterized by scanning electron microscopy (SEM), atomic force microscopy (AFM), and energy-dispersive X-ray spectroscopy (EDS). The resulting CuNP patterns feature porous 3D microdomains with nanometric structures serving as hot spots for Raman signal enhancement. Low-temperature post-treatment (below 200 °C) of the deposited CuNPs significantly evolves its morphology and leads to sintering of NPs into a semicrystalline structure with sharp geometric features, which resulted in a more than 10-fold increase of the enhancement factor (up to 2.1 × 10^5) compared to non-heat-treated samples. The proposed method allows creating SERS substrates constituted by sharp 3D metallic nanopatterns selectively deposited onto specific regions, which paves the way for new printed, highly sensitive SERS-based sensors.

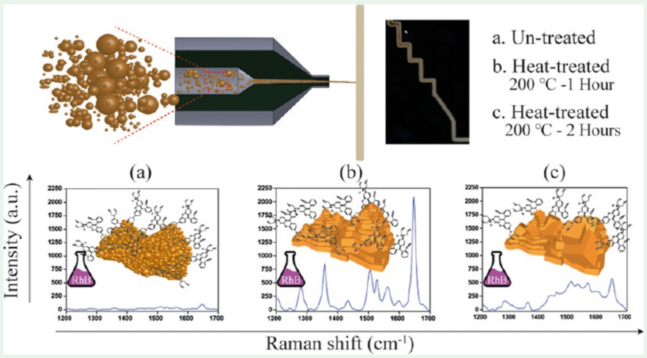

KEYWORDS: *surface-enhanced Raman scattering (SERS), aerosol direct writing, copper nanoparticle, spark ablation method (SAM), thermal treatment*

1. INTRODUCTION

Surface-enhanced Raman scattering (SERS) spectroscopy is a rapid, label-free, and straightforward technique employed in many applications ranging from low concentration and even single-molecule detection[1,2] to DNA studies[3] due to its ability to provide a variety of information about chemical and structural features of different species. SERS is widely used in many fields such as biology,[4] material science,[5] food analysis,[6] and medicine[7] and is based on the amplification of the Raman signal by several orders of magnitude taking place on metallic nanostructured surfaces and enabling ultrasensitive fingerprinting of molecules.

In the amplification of the Raman signal, two primary mechanisms must be taken into account: chemical enhancement and electromagnetic enhancement.[8] The chemical enhancement is highly molecule specific[9] and is primarily related to charge transfer mechanisms between the molecule and the metal. The other enhancement mechanism, which has the highest impact on the total enhancement, is the electromagnetic (EM) one.[10] The EM enhancement of the Raman signal is due to localized surface plasmon resonance (LSPR) taking place at the surface of metal particles featuring nanometric roughness.[5] These excitations are due to collective oscillations of the electron cloud in the presence of incident light at the interface between a metal and a dielectric. Surface plasmons are localized because of their confinements within the surface of a nanoparticle (NP) or on edges and corners of a metallic nanostructure. The results of this confinement are (1) selective photon absorption depending on the size and shape of the nanostructure and (2) amplification of the EM field.[11] The regions of a surface with the ability to enhance the Raman signal are termed hot spots.[12]

Noble metals, such as silver[13,14] and gold,[15,16] structured with feature sizes of few nanometers to hundreds of nanometers and having LSPR in the visible regions of the spectrum, are widely employed as SERS-active substrates. Alternatively, copper, a less expensive material, is another metal employed in SERS-active substrates; it generally leads to lower Raman enhancement compared to substrates made of

Received: April 3, 2020
Accepted: May 27, 2020
Published: May 27, 2020

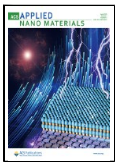

https://dx.doi.org/10.1021/acsanm.0c00887
ACS Appl. Nano Mater. 2020, 3, 5665−5675

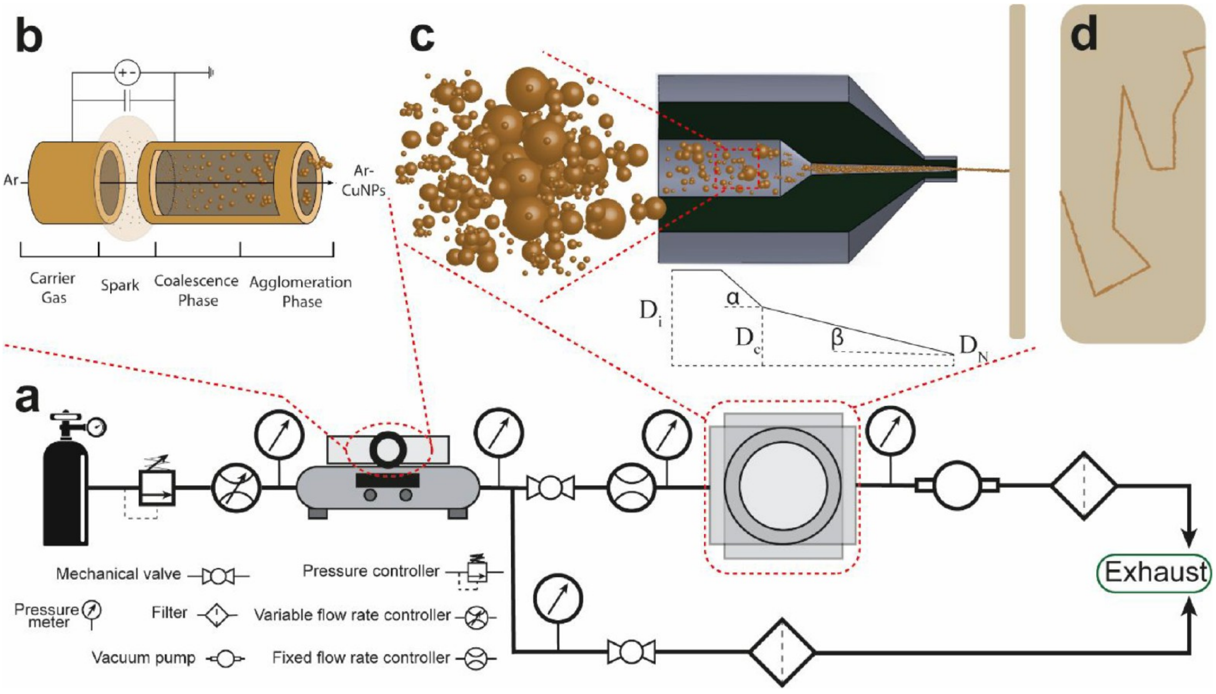

Figure 1. Schematic representation of (a) the aerosol direct writing system and its components. (b) Spark ablation method working principle. (c) NPs and agglomerates of NPs focusing in a long converging nozzle and axisymmetric view of the nozzle and its configuration. (d) Example of a deposited NP pattern.

gold or silver. The low SERS effect of a Cu SERS substrate can be compensated by using a 3D structure instead of a 2D configuration to increase the number of hot spots. The presence of a 3D structure also increases the number of adsorbed probe molecules around the hot spots due to the higher surface area. Different strategies have been developed for manufacturing SERS-active substrates such as chemical reduction,[17,18] self-assembly,[19,20] screen printing[21] electrochemical deposition,[22,23] dealloying or decomposition,[24] thermal decomposition,[25] and nanosphere lithography (NSL).[26] All these methods are characterized by either multistep processes, high temperature, high level of vacuum, presence of hazardous chemicals, or expensive instruments. Furthermore, these methods create SERS-active regions all over the surface; however, for the integration of SERS into a sensor or a microfluidic device, it would be desirable to have SERS-active patterns in a specific location. To fabricate local SERS-active patterns, methods such as electron beam lithography (EBL)[27] and photolithography[28] can be employed to create nanopatterns in the desired location with high control over the shape, size, and spacing of hot spots; however, they are expensive, time-consuming, and limited to typical semiconductor material systems. In this work, we report an innovative approach allowing selective direct writing of copper nanoparticle patterns via aerosol direct writing (ADW) and heat treatment of the deposited film to tune and significantly improve the SERS signal enhancement.

In ADW, an in-line spark ablation method (SAM) is used to generate metal or alloy NPs,[29,30] which are deposited in well-defined regions of the substrate by using an aerodynamically focusing system. The deposited pattern is composed of 3D nanoparticles' microstructures featuring a height of hundreds of nanometers with high porosity and nanometric roughness. We also report how the tuning of process parameters, such as the deposition speed and nozzle to substrate distance, has a direct influence on the width of the pattern and the density of the nanoparticles. Furthermore, we show that the morphology of the deposited film is significantly affected by a low-temperature thermal post-treatment (below 200 °C), converting the porous structure into multifaceted microdomains with sharp corners and edges. A low-concentration analyte, Rhodamine (RhB), is used to study the tunability of the SERS signal enhancement in relation to the evolution of the CuNP film morphology. Compared to untreated samples, a SERS signal enhancement of more than 1 order of magnitude was achieved.

2. EXPERIMENTAL SECTION

2.1. Aerosol Direct Writing. An experimental setup (aerosol direct writing (ADW)) was used for the spatially selective deposition of copper nanoparticles (CuNPs), consisting of a commercial particle generator (VSParticle G1) and a deposition unit as illustrated schematically in Figure 1a. The particle generator exploits the spark ablation method (SAM) (Figure 1b). In the SAM, the discharge of electrons (sparks) between two electrodes (copper 99.99% pure) generates a locally high temperature (typically 20000 K[31]) at the spark location.[32,33] The introduced energy leads to local evaporation of the electrode material. The vapor is carried away by an inert gas (argon), controlled by a Bronkhorst HighTech El-Flow Prestige (inlet volumetric flow rate between 150 and 20000 sccm), and is quenched very shortly after its evaporation by passing through an orifice in the system, which causes the metal vapor to cool and coalesce into primary spherical NPs[34] (10^9–10^{12} cm^{-3} particles, polydispersed mixture with particle sizes between 0 and 20 nm[32]). After that, the NPs start to form agglomerates of diverse shape and size (tens to hundreds of nanometers) by particle–particle interaction and impaction. The parameters to control particle size and amount are the frequency of the electrical field, the current, and the argon gas flow.

The deposition unit consists of a vacuum chamber, a dry pump, a converging nozzle for focusing the beam of particles, and a stage to move the substrate along the plane perpendicular to the gas and particle flow. The focusing nozzle consists of a converging section with a 10 mm diameter inlet (D_i) and half-angle of 45° (α) followed by a 20 mm converging capillary nozzle (L_c) with a 2 mm diameter inlet (D_c) and half-angle of 2° (β) ending in a 400 μm diameter throat (D_N) representing the outlet of the focusing nozzle (Figure 1c). The nozzle is designed in SOLIDWORKS and manufactured by using an Envisiontech Micro plus high-resolution stereolithographic 3D printer with 25 μm resolution and postprocessed by UV-curing for 3 min.

Concerning the fabrication of patterned active-SERS substrates, 1 in. sized silicon substrates, cleaned with acetone and isopropanol, are mounted on the stage in the vacuum chamber. The stage controller consists of two SmarAct SLC-1750-M-E-HV positioners for patterning of a substrate with in-plane motions (X, Y) of the stage and one SmarAct SLC-1750-O20-D-HV positioner for out-of-plane motion (Z) of the stage to precisely control the distance of the nozzle to substrate. For each nozzle-to-substrate distance, three samples were prepared by printing CuNP on a clean silicon substrate with a flux of 930 sccm, 1 bar upstream pressure, vacuum pressure of 270 ± 1% Pa, deposition writing speed of 50 μm s^{-1}, and SAM voltage and current setting of V = 1.2 kV and I = 8 mA, respectively. Concerning the thermal post-treatment, the silicon substrates with CuNPs patterns were placed in a Binder VD23 vacuum oven with a vacuum pressure of 0.01 mbar.

2.2. Morphology Characterization. The morphology of the patterned area was characterized by scanning electron microscopy (SEM), atomic force microscopy (AFM), and optical microscopy (OM). The SEM measurements were performed with the following SEM microscopes: Jeol JSM-6010LA, field-emission high-resolution Jeol JSM-6500F, and FEI NovaNano, all with a secondary electron detector. The elemental analysis of deposited patterns was performed through an energy-dispersive X-ray spectrometer integrated into the SEM Jeol JSM-6010LA setup at a magnification of 2500 and acceleration voltage of 15 kV. For each configuration of heat treatment (no heat treatment, 1 h at 100 °C, 1 h at 200 °C, and 2 h at 200 °C), four EDS analyses were performed randomly in the centric regions and two in the boundary zones. The optical pictures were recorded with a Keyence digital microscope (VHX-6000) able to magnify from 20× to 2000×. The HDR (high dynamic range) function, allowing to capture multiple images at varying shutter speeds, improved the resolution and the contrast between substrate regions with and without deposited CuNPs. The boundary of the line was therefore chosen as the region where there was a clear difference in the contrast. For each distance between the nozzle and the substrate, the width of three lines printed on three silicon substrates was measured.

The AFM measurements were performed by a JPK Nanowizard 4 coupled to a Zeiss microscope in QI mode. Silicon tips TESPA-HAR with the resonant frequency of 320 kHz, force constant of 42 N m^{-1}, a high aspect ratio of at least 5:1, and a curvature radius of 10 nm were used. The high aspect ratio of the tip enables the imaging of surfaces with high differences in height, reducing possible tip−sample convolution artifacts. Three scan areas of 3.0 × 3.0, 1.5 × 1.5, and 0.5 × 0.5 μm^2 were used to study the morphology of the samples. All AFM measurements were performed in air at room temperature and were leveled with linear subtraction of background data for both horizontal and vertical lines by using GWYDDION 2.55 software.

2.3. SERS Measurements. Concerning SERS studies, a Rhodamine B (RhB) solution with a concentration of 1.0 × 10^{-6} M was prepared out of RhB powder, purchased from Sigma-Aldrich, and deionized water. To ensure a homogeneous distribution of the probe molecule on the nanostructured surface, an immersion method was used. The samples were immersed in the RhB solution for 12 h to ensure sufficient molecule adsorption on the samples. After that, the samples were removed from the solution, washed thoroughly with deionized water to remove the excess of RhB, and dried with a nitrogen stream. Compared to droplet-on-substrate deposition protocols, our approach prevented "coffee-stain effects" that could lead to the accumulation of the probe molecules at the edge of a drying droplet deposited on the substrate.[35] Concerning Raman spectroscopy measurements, a Horiba LabRAM HR setup, equipped with an argon ion laser operating at 488, 514, and 633 nm, a CCD camera, and a 50× (NA = 0.5) objective was used. All SERS spectra were acquired with the laser operating at 514 nm at a power of 20 μW, with an acquisition time of 30 s, and an average laser beam spot size of about 2 μm measured on bare silicon, unless mentioned otherwise. The spectra were collected over the range of 500−1700 cm^{-1} with a spectral resolution of ∼0.3 cm^{-1}. The spectral data were recorded by using LabSpec6 software, and baseline correction was performed to remove the fluorescent background. To assess the level of reproducibility of SERS signal on the fabricated patterns, the Raman signal of RhB on CuNPs deposited patterns with and without heat treatment was measured at 18 different locations within the patterns.

3. RESULTS AND DISCUSSION

Figure 1c shows the schematic of a designed focusing nozzle, which enables the experimental setup to deposit CuNPs selectively on the substrate. The focusing nozzle accelerates the carrier gas and propels the particles due to the pressure difference between the upstream (P_u) and downstream (P_d) of the nozzle. The ratio of the upstream to downstream pressure (vacuum pressure) of the nozzle defines the mode of flow at the outlet of the nozzle: subsonic, sonic, or hypersonic.

A pressure ratio (P_d/P_u) lower than 0.49 ($P_d/P_u = (2/\gamma + 1)^{\gamma/(\gamma-1)}$, with γ = 1.66 for argon[36]) causes a sonic flow mode. Further decrease in the pressure ratio leads to a strong expansion of the gas outside of the nozzle and enables the gas to reach higher velocities. When this expansion of gas impinges onto a plate, a stagnation plane is created in front of the plate by the so-called bow shock. Across the bow shock, a sharp difference in pressure and velocity of gas appears with a zero velocity on the plate. The nanoparticles' velocity is affected significantly by any change in the flow because of their low inertia; therefore, they can reach higher velocity outside the nozzle in the expansion zone of the gas. This allows them to leave the streamline and deposit on the target substrate. The highest pressure ratio between upstream and downstream of the nozzle takes place when a stagnation point at atmospheric pressure (10^5 Pa) and clean room temperature (293 K) is reached, and the vacuum pump works at its highest power. In this configuration, the flow rate controller is set at 930 sccm, the vacuum pressure is equal to 270 ± 2% Pa, and the pressure ratio is $377^{-1} < P_d/P_u < 363^{-1}$.

The other parameter affecting the expansion of the gas after the nozzle and further deposition of the NPs on the substrate is the distance between the nozzle and the substrate. A small distance causes a weaker gas expansion and lower gas and particle velocity. On the other hand, a high distance leads to not only a fully expanded gas and high particle velocity but also a higher distance of bow shock to the substrate. This further increases the traveling path of particles to reach the substrate and, consequently, reduces the chance of deposition. Figure 2a1−a8 shows the optical microscopy images of the variation in the width of the deposited line according to different distances between the nozzle and the substrate.

Figure 2b shows that the width of the lines depends on two factors: the distance between the nozzle and the substrate and the diameter of the nozzle. Increasing the distance of the nozzle to the substrate from 200 μm (0.5 × D_N) to 1600 μm (4.0 × D_N) leads to an increase in the width of the line from 265 μm ± 2% (∼0.65 × D_N) to 505 μm ± 2% (∼1.25 × D_N). Increasing the width of the line also leads to a decreasing density of the particles and less uniform deposition; however, this can be compensated by increasing deposition time. The

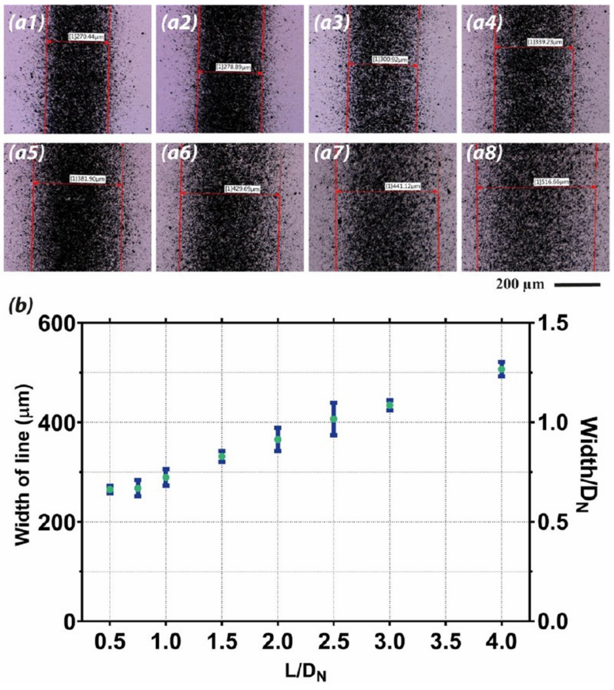

Figure 2. Optical microscopy of the variation of the width lines at a nozzle-to-substrate distance of (a1) 200, (a2) 300, (a3) 400, (a4) 600, (a5) 800, (a6) 1000, (a7) 1200, and (a8) 1600 μm. (b) Relationship between the width of the deposited line and the ratio between the nozzle-to-substrate distance and the nozzle diameter (L/D_N). For each distance between the nozzle and the substrate, the width of three lines printed on three silicon substrates was measured by using HDR images. All lines were printed on silicon substrates with a flux of 930 sccm, 1 bar upstream pressure, the vacuum pressure of 270 ± 1% Pa, deposition writing speed = 50 μm s^{-1}, nozzle throat of 400 μm, and SAM voltage/current setting of $V = 1.2$ kV and $I = 8$ mA.

results show that by controlling the distance of the nozzle to substrate and the time of deposition, it is possible to create patterns with various widths in the range of the diameter of the nozzle. In further studies, we will consider the fabrication of nozzles with smaller diameters. Although all the SERS experiments in this work were performed on Si surfaces, the direct writing methodology has also been validated on other kinds of substrates (Figure S1).

Figure S2a and Figure 3a show a film of copper nanoparticles (CuNPs) deposited on a silicon substrate and the typical morphology of the film in low-magnification SEM images. The agglomerates of NPs with different shapes and sizes, together with primary NPs in various sizes, formed a dense layer on the substrate that contains valleys and hills in a three-dimensional (3D) configuration (Figure 3b). A closer look at the structure of the film is provided in Figure S2d,e with a high-resolution SEM and by AFM images depicted in Figure 4a,b. We observe that the 3D structure is composed of a random network of very fine NPs featuring a spongelike morphology characterized by high porosity and surface area. Apart from NPs and agglomerates of NPs deposited on the substrate, Figure 3a indicates the presence of microparticles with size ranging from hundreds of nanometers to few micrometers. Microparticles result from the solidification of larger units of molten metal occasionally ejected from the surface of the electrode into spherical particles,[32] such as the microparticle shown inFigure S2f. The number of these microparticles in regions close to the center of the line (Figure S2a) is higher than in regions closer to the boundary of the line (Figure S2b) since microparticles have higher mass and consequently higher inertia compared to NPs.

The evolution of the surface morphology by different thermal post-treatments is shown in Figures 3c−h and 4c−h. The melting temperature of nanoparticles (T_{NP}) and their sintering temperature are a function of the nanoparticle's size (D_{NP}) and decrease drastically from the bulk melting

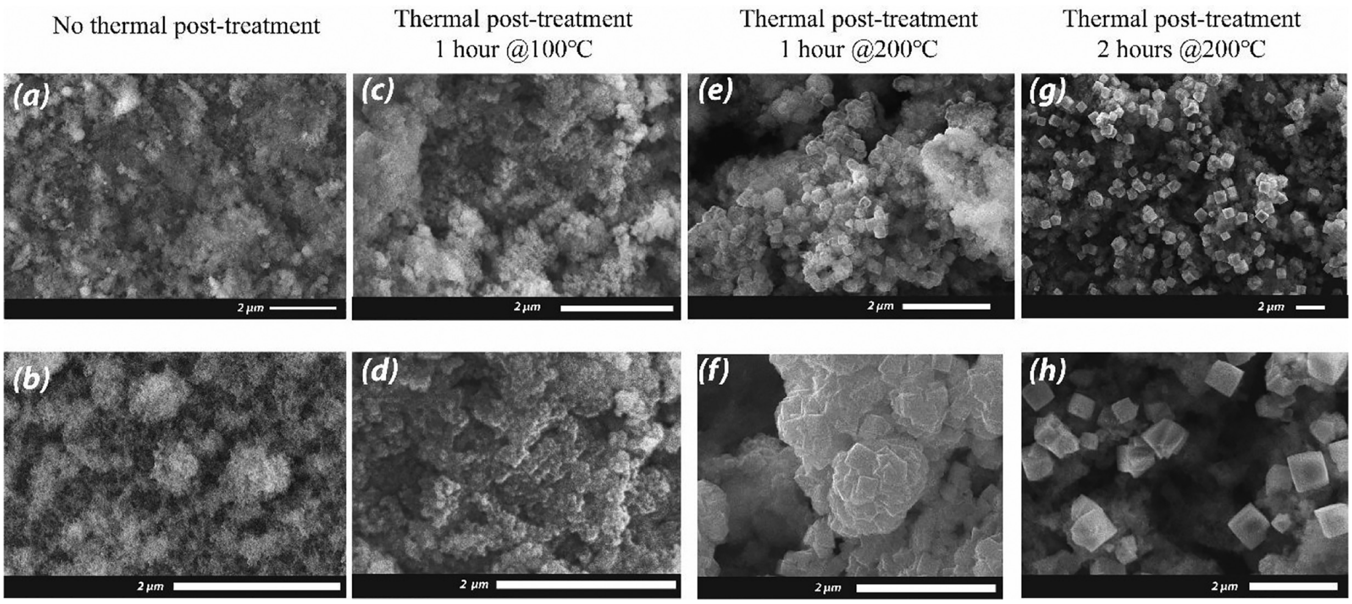

Figure 3. (a, b) SEM images of the morphology of CuNPs, agglomerates, and Cu microparticles deposited on the silicon substrate. (c, d) Transformation of the CuNPs deposited on a silicon substrate to crystalline form after thermal treatment in the vacuum oven for 1 h at 100 °C. (e, f) After thermal treatment in the vacuum oven for 1 h at 200 °C. (g, h) Crystal growth after thermal treatment in the vacuum oven for 2 h at 200 °C. All CuNPs deposited with SAM voltage/current setting of $V = 1.2$ kV and $I = 8$ mA.

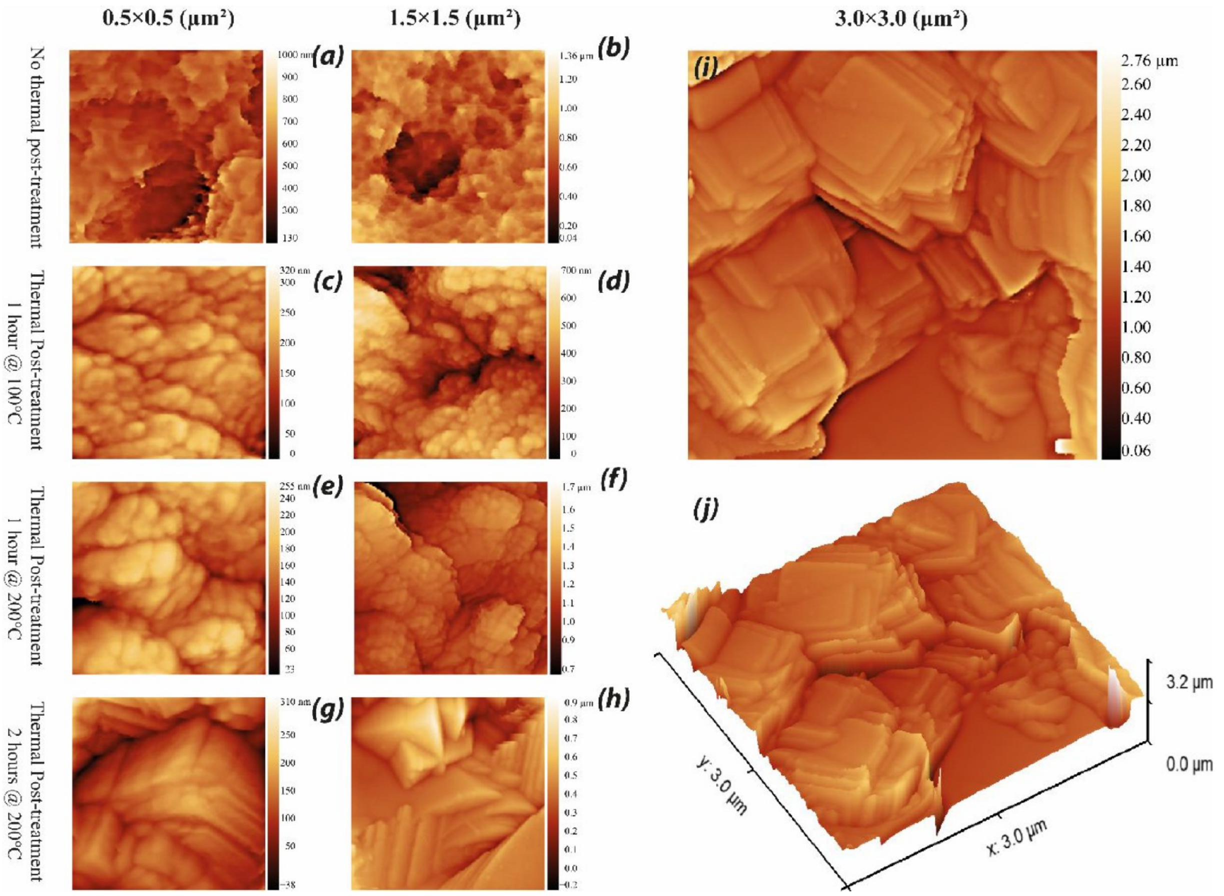

Figure 4. AFM morphology of 0.5 × 0.5 and 1.5 × 1.5 μm^2 areas of (a, b) samples without heat treatment, (c, d) samples heat-treated at 100 °C and 1 h, (e, f) samples heat-treated at 200 °C and 1 h, (g, h) samples heat-treated at 200 °C and 2 h. AFM morphology of (i) 3.0 × 3.0 μm^2 area of the thermal post-treated sample at 200 °C and 2 h in the vacuum oven and (j) its 3D view. All CuNPs deposited with SAM voltage/current setting of $V = 1.2$ kV and $I = 8$ mA.

temperature (T_{Bulk}) following the law $(T_{\mathrm{NP}} - T_{\mathrm{Bulk}})/T_{\mathrm{Bulk}} = f(-1/D_{\mathrm{NP}})$.[37−39] The dependence of the melting temperature of nanoparticles on their size is particularly important for particles with a size below 20 nm.[39] The SEM images (Figure 3c,d) and AFM images (Figure 4c,d) show that the 3D spongelike structure, composed by individual CuNPs, starts to sinter at a temperature of 100 °C and transforms into a compacted structure with micrometric 3D domains containing particulate shapes of tens of nanometers and lower porosity compared to non-heat-treated samples.

The surface morphology of deposited CuNPs and heat-treated in a vacuum oven for 1 h at 200 °C is depicted in Figure 3e,f. The AFM images of Figure 4e,f show that the thermally treated sample at 200 °C features a morphology similar to the ones treated at 100 °C but with larger particulate sizes. Figure S3d and Figure 3f show that the 3D micrometric domains contain corners and edges with a size ranging from tens of nanometers to a maximum of 200 nm.

Increasing the sintering time to 2 h provokes further fusing of CuNPs into larger shapes and ordered structures, as shown in Figures 3g,h and 4g,h. The previously formed compacted 3D structures after 1 h treatment at 200 °C undergo further reordering, leading to multifacet 3D aggregates with size between hundreds of nanometers until a maximum of 2 μm, as shown in Figure 4i,j. The frequency of the presence of these cubic copper aggregates decreases by moving from the center of the line toward the boundaries, as shown in Figure S4a (the right sides of both pictures are closer to the center of the line). In the boundary regions, CuNPs turned into aggregates with micrometric size; however, they have a less ordered shape compared to cubic aggregates present in the centric regions (Figure S4b−d). This difference in the microstructure of the thermally treated CuNPs at different positions of the line may be related to the differences in the amount of material present in the centric regions compared to the boundary of the line. This lack of material in the boundary region limits the formation of larger and more-ordered aggregates. The other possible explanation might be related to the presence of copper with different oxidation states at the surface in different regions of the line.

To quantify the presence of oxidations states, we performed an elemental analysis of the fabricated samples by using energy-dispersive X-ray spectrometry (EDS, see the Supporting Information, Table S1 and Figure S5) on two regions: in the centric regions of the line with higher CuNPs coverage over the deposited area and in the boundary regions featuring lower CuNPs coverage. The EDS results reported in Table S1 show the presence of copper, oxygen, silicon, and carbon. The presence of silicon in the elemental analysis is due to the penetration of the X-ray into the film until the silicon substrate. Its presence is therefore lower in the inner regions compared to the boundary ones due to the higher coverage of CuNPs and higher thickness of the film. The EDS analysis of a silicon substrate without CuNPs is shown in Figure S5a and highlights the only presence of silicon without any trace of carbon. Therefore, we attribute the presence of carbon in the CuNPs deposited substrates to the reaction of copper nanoparticles with CO_2 in the air. It should be noted that oxidation of copper occurs very shortly after it is exposed to air because of the chemical reactivity of CuNPs[40] and the relatively low thickness of CuNPs film. Figure 5 shows the ratio of copper to oxygen in the CuNPs deposition at the boundary of the deposition area and within inner regions of the line.[41] The sample without heat-treatment shows that the centric regions oxidized uniformly, leading to the formation of copper(II) oxide (CuO); however, the boundary has a higher oxygen ratio compare to inner regions.

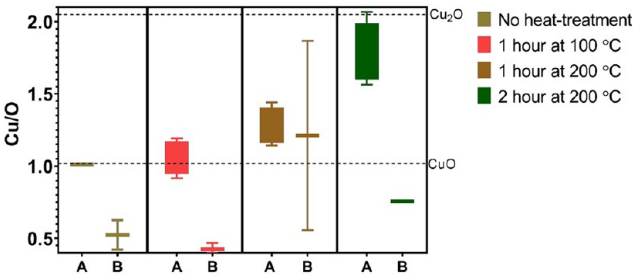

Figure 5. Elemental ratio of copper to oxygen in different samples: (A) inside the line and (B) boundary of the line.

To evaluate the effect of heat treatment on the elemental compositions of the samples, the EDS characterization was also performed on heat-treated samples. As shown in Figure 5, the centric regions for almost all samples have a higher ratio of copper to oxygen compared to boundary regions. This ratio starts to increase in the centric regions with an increase of time or temperature of the thermal treatment, which is an indication of the transformation of the CuO to Cu_2O. Unlike bulk copper oxide (CuO), which reduces directly to copper, the CuO nanoparticles first completely reduce to Cu_2O by ($4CuO(s) \rightarrow 2Cu_2O(s) + O_2(g)$) and then to Cu ($2Cu_2O(s) \rightarrow 4Cu(s) + O_2(g)$),[42,43] which is a reaction that requires a temperature higher than 200 °C.[44] The Cu_2O is a stable compound of copper with cubic crystalline structure;[45] therefore, the gradual increase in the ratio of copper to oxygen in the centric regions from 1 to 2 leads to a transformation of the nanostructure from spherical shape to larger cubical shape. The higher ratio of oxygen to copper in the boundary regions might relate to the presence of finer nanoparticles with a higher surface area.

According to the morphology characterization results mentioned above, the film of CuNPs features high roughness and a spongelike 3D morphology containing nanostructures with a size distribution between 0 and 20 nm. To evaluate the SERS performance, a series of Raman experiments were performed by using low-concentration Rhodamine B (RhB) as a probe molecule. The schematic of a typical deposited CuNPs line on a silicon substrate is shown in Figure 6a. For each experiment, the width of a line is divided into six regions, and in each region, three Raman acquisitions on three different points are performed. The Raman points are specific regions in the cross section of the deposited line, which are chosen because of their clearly distinct morphology. In this configuration, the Raman signal of RhB was measured at 18 different points to assess the level of reproducibility of the SERS signal on the fabricated patterns. Rhodamine B (RhB) with a concentration of 1.0×10^{-6} M was adsorbed on the CuNPs deposition and showed a distinguishable Raman signal under laser excitation at 514 nm. The SERS effect is higher when the laser excitation promotes the LSPR on the metal nanostructure. However, the laser excitation options of Raman equipment have limited options, and for complex nanostructures, LSPR occurs at multiple wavelengths due to the presence of higher-order multipole plasmonic modes.[46] In this study, a combination of theoretical calculations based on the Mie theorem for very fine spherical copper nanoparticles[47] and a series of experiments on complex nanostructures was employed to find the best laser excitation, which is 514 nm. The procedure is explained in detail in section 4 of the Supporting Information. The characteristic Raman spectrum of RhB is shown in Figure 6b with its most important peaks: 621 cm^{-1} (for xanthene ring puckering), 1199 and 1279 cm^{-1} (for C−C bridge band stretching and aromatic C−H bending), 1358 cm^{-1} (for aromatic C−C bending), 1505 and 1528 cm^{-1} (for aromatic C−H bending), and 1648 cm^{-1} (for aromatic C−C bending and C=C stretching). In Figure 6b, at 520.7 cm^{-1}, the silicon peak is also shown, and it is present in the SERS spectrum of RhB if the CuNPs deposited line is not thick

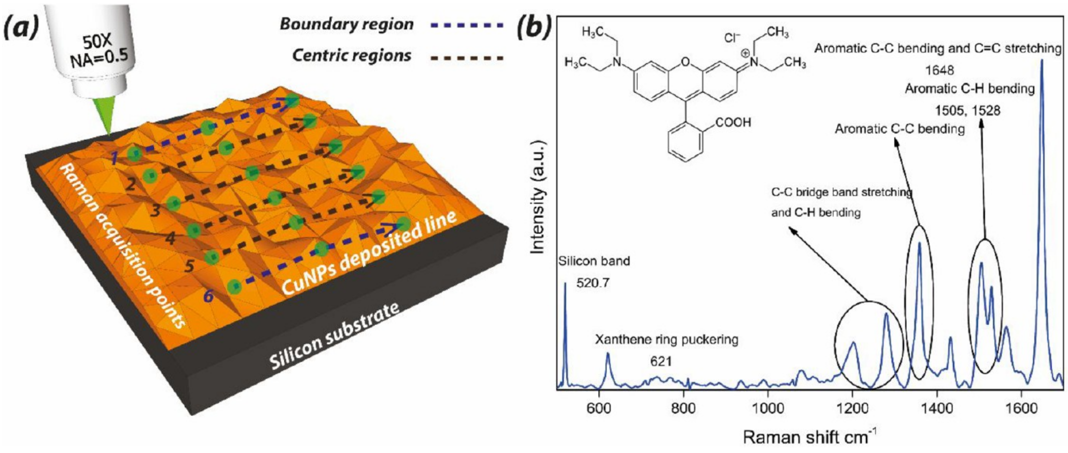

Figure 6. (a) Schematic view of the typical Raman acquisition map over a deposited line (the green circles are the acquisition points). (b) Raman spectrum Rhodamine B. Raman measurement conditions: argon ion laser operating at 514 nm and power of 20 μW; acquisition time = 30 s; objective lens = 50× (NA = 0.5).

https://dx.doi.org/10.1021/acsanm.0c00887

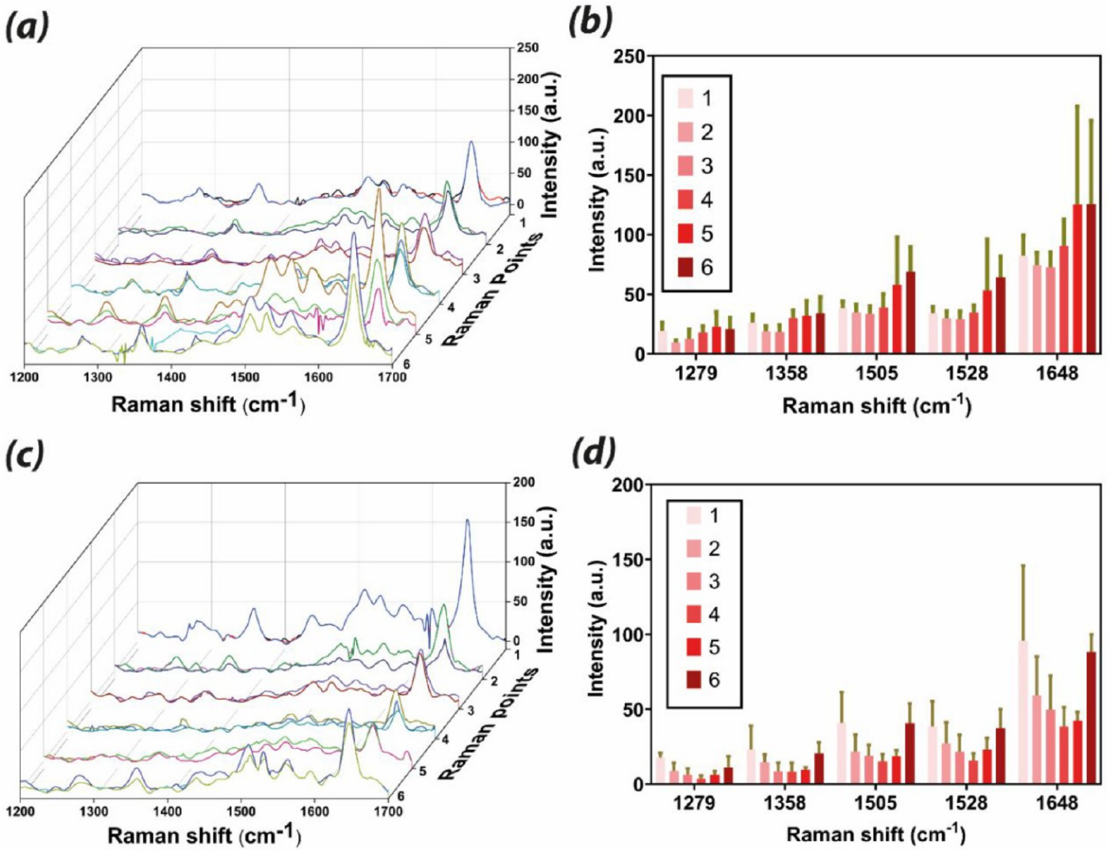

Figure 7. (a, c) Raman spectra of 1.0 × 10^{-6} M RhB on CuNPs patterns obtained at writing speeds of 10 and 2 μm s^{-1}, respectively, for 18 points in six regions. (b, d) Averaged intensities of main peaks of RhB for each of the six Raman regions corresponding to Raman spectra of (a) and (c), respectively. Raman measurement conditions: argon ion laser operating at 514 nm and power of 20 μW; acquisition time = 30 s; objective lens = 50× (NA = 0.5).

enough to cover the silicon substrate completely. For SERS characterization, the five peaks of RhB (1279, 1358, 1505, 1528, and 1648 cm^{-1}) were considered.

The first set of experiments are related to the adsorption of RhB on the patterns of CuNPs deposited on a silicon substrate with SAM setting of 1.2 kV and 8.0 mA and a fixed nozzle-to-substrate distance of 400 μm ($L/D_N = 1$). Figure 7a,c reports 18 Raman spectra of RhB on CuNPs deposited on the silicon substrate with two writing speeds of 10 and 2 μm s^{-1} in the spectral range of 1200−1700 cm^{-1}.

The values on the oblique axes in Figure 7a,c relate to regions shown in Figure 6a and contains three Raman acquisitions for each region. The distribution of the five main characteristic peaks of RhB for the six Raman points is shown in Figure 7b,d. The spectra acquired on NPs patterns fabricated at both writing speed show that 1.0 × 10^{-6} M RhB is detectable, and all characteristic peaks of RhB are observable with the highest peaks at 1648 cm^{-1}. Furthermore, Figure 7b,d shows that the highest intensities for each peak of RhB occur in the region far from the center and closer to the boundary. We tentatively attribute this to the lower surface area and lower LSPR in the centric regions, which contain a higher number of microparticles.

The effect of thermal post-treatment with different times and temperatures on the enhancement of the Raman signal of 1.0 × 10^{-6} M RhB is shown in Figure 8. Comparing the Raman spectrum of 1.0 × 10^{-6} M RhB adsorbed on non-heat-treated CuNPs to the heat-treated ones for 1 h at 100 °C (respectively Figures 7a and 8a), it is clear how the SERS intensity is amplified on average by a factor 4. Thermal treatment of CuNPs at 100 °C triggers the sintering of the fine nanoparticles into larger structures, although the temperature or the heating time are not sufficient for inducing a significant coalescence of the NPs. The SERS intensity is further improved by increasing the temperature of the vacuum oven from 100 to 200 °C (Figure 8b), which averagely enhanced the signal intensity by a factor 10 compared to the non-heat-treated CuNPs. Thermal treatment of CuNPs at 200 °C for 1 h leads to the formation of aggregates with larger nanofeature size, as shown in Figure 3e,f, and this induces a red-shift in the LSPR[48−50] of copper structures and therefore a better amplification of electromagnetic wave and consequently Raman signal.

The prolongation of the heat treatment at 200 °C from 1 to 2 h leads to a significant decrease of the SERS intensity in the centric region of the line and an increase in the boundary regions (Figure 8c). As mentioned above, the morphology of the thermally treated CuNPs in the centric regions treated at 200 °C for 2 h is characterized by the presence of large cubic aggregates with a feature size of several hundreds of nanometers and less effectiveness as a hot spot for the enhancement of the SERS signal.

The other hindering point of oversintered CuNPs relates to a decrease in the surface area of the microstructure due to fusing NPs hence lower area for adsorption of RhB molecules. As shown for the SERS signal of RhB on CuNPs without heat

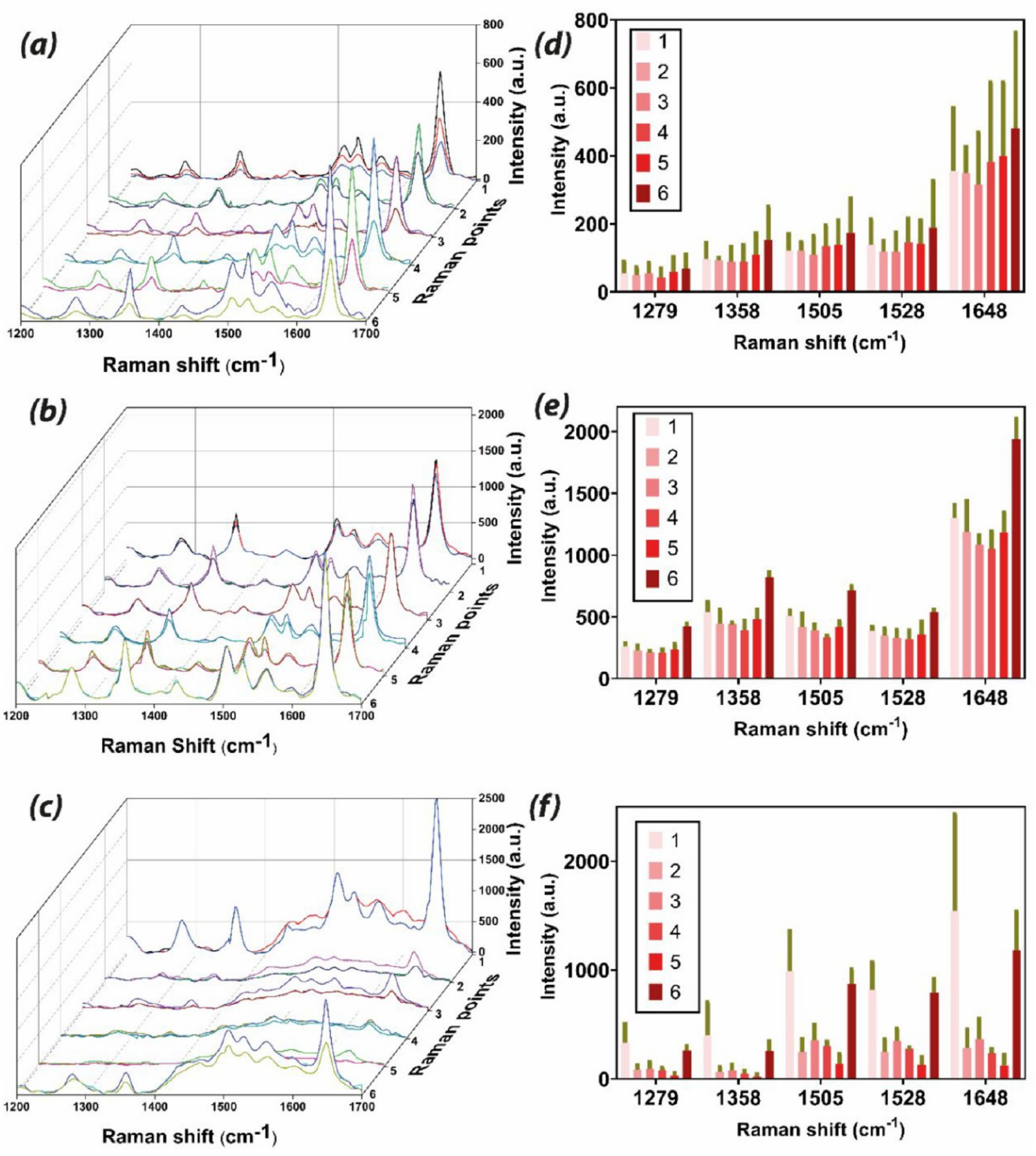

Figure 8. Raman spectra of 1.0 × 10^{-6} M RhB on CuNPs patterns obtained at writing speed of 2 μm s^{-1} and (a) 1 h thermal treatment of 100 °C, (b) 1 h thermal treatment of 200 °C, and (c) 2 h thermal treatment of 200 °C in a vacuum oven (18 points in six regions). (d, e, f) Averaged intensities of main peaks of RhB for each of the six Raman regions corresponding to the Raman spectra of (a, b, c), respectively. Raman measurement conditions: argon ion laser operating at 514 nm and power of 20 μW; acquisition time = 30 s; objective lens = 50× (NA = 0.5).

treatment, the highest intensities for heat-treated samples take place as well at the boundary of the deposited line. This phenomenon can be explained by the presence of a higher number of edges and corners in the structures closer to the boundaries of the heat-treated CuNP films.

The enhancement factor (EF), a quantitative parameter to compare the efficiency of active SERS substrates, was calculated based on the intensity of the 1648 cm^{-1} peak, which is the most intense spectral feature of RhB, by using the following equation:[51−54]

$$\mathrm{EF} = \frac{I_{\mathrm{SERS}}}{I_0} \times \frac{C_0}{C_{\mathrm{SERS}}}$$

where I_{SERS} and I_0 are the intensities of the 1648 cm^{-1} peak for C_{SERS} = 1.0 × 10^{-6} M and C_0 = 1.0 × 10^{-3} M RhB, respectively. For calculating the EF, a reference sample was prepared by immersing a bare silicon substrate in a 1.0 × 10^{-3} M (1 mM[55]) RhB solution for 12 h, and I_0 was measured three times and averaged to a value of ~7.317 au (Figure S9). Figure 9 shows the evolution of the EF, taking into account 18 Raman points on different regions of the patterns for samples with and without thermal post-treatment. The highest EF is 2.1 × 10^5, and the highest averaged EF is 1.6 × 10^5 for the heat-treated samples at 200 °C for 1 h; moreover, these samples show the best reproducibility and lowest standard deviation compared to other samples. This value is comparable to other reported copper-based SERS-active substrates[18,56,57] and is close to the EF of gold SERS substrates[58,59] and silver SERS substrates.[60] These results indicate that the SERS features of CuNPs, selectively deposited on a substrate by aerosol direct writing, can be significantly enhanced via thermal post-treatment up to a level comparable with one of other noble metals.

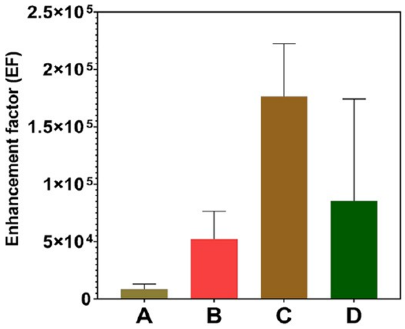

Figure 9. Average enhancement factor (EF) for (A) non-heat-treated sample, (B) thermal post-treatment at 100 °C for 1 h, (C) thermal post-treatment at 200 °C for 1 h, and (D) thermal post-treatment at 200 °C for 2 h. All CuNPs were deposited with a SAM voltage/current setting of $V = 1.2$ kV and $I = 8$ mA and writing speed of 2 μm s^{-1}. Raman measurement conditions: argon ion laser operating at 514 nm and power of 20 μW; acquisition time = 30 s; objective lens = 50× (NA = 0.5).

4. CONCLUSIONS

In this work, we proposed a novel, simple, and solvent-free direct writing method for the selective deposition of micrometric metal (copper) nanoparticles' patterns, and we demonstrated their application as SERS sensors. By varying the parameters of the writing process and by introducing a thermal post-treatment, we were able to tune the morphology of the deposited patterns and significantly enhance the Raman signal of a reference dye (Rhodamine B). The selectively deposited films were composed by a collection of dense spherical primary particles with various sizes. The smallest line-width that we achieved was equal to 265 μm and largely depends on the size of the 3D printed nozzle. Narrower patterns can be achieved in future through high-resolution laser-assisted 3D printing (laser stereolithography[61] or two-photon polymerization[62]) of nozzles featuring smaller orifices. The deposited patterns of copper NPs with sponge-like structures allowed the detection of 1.0×10^{-6} M concentration of RhB. A low-temperature thermal post-treatment at 100 °C for 1 h triggered a transformation of the microstructures by fusing nanoparticles into larger nanostructures. This transformation of the film morphology caused an enhancement of the Raman signal of RhB. The highest enhancement of the Raman signal of RhB was achieved with a thermal treatment at 200 °C for 1 h (EF $\approx 2.1 \times 10^5$). Increasing the time of thermal treatment from 1 to 2 h at 200 °C, resulted in a decrease of the Raman signal intensity and a further change of the morphology into microparticulate structures induced by the fusion of the nanoparticles. A great advantage of this method is the ability to selectively deposit metal and alloy NPs patterns with a 3D microstructure on different kinds of substrates (Si, glass, and paper). This feature could allow in the future to integrate metallic nanofeatures within specific regions of microfluidic devices. At the same time, the easy tunability of the nanometallic morphology through process parameters, the possibility to extend the method to other more performing materials (e.g., Au and Ag), and its integrability with other fabrication methods, paves the way for the realization of new SERS sensors.

ASSOCIATED CONTENT

Supporting Information

The Supporting Information is available free of charge at https://pubs.acs.org/doi/10.1021/acsanm.0c00887.

> Optical image of possible patterning on different substrates, SEM and HR-SEM images of the samples with and without heat treatment, EDS spectra of different samples, extinction cross-section calculation for nanoparticles, Raman spectra of RhB on samples with and without heat treatment under excitation laser of 488, 514, and 633 nm, Raman spectra of RhB on samples patterned with higher deposition velocity and Raman spectra of RhB with a concentration of 1 mM on bare silicon as a reference sample (PDF)

AUTHOR INFORMATION

Corresponding Author

Saleh Aghajani − *Delft University of Technology, Faculty of Mechanical, Maritime, and Materials Engineering (3ME), Department of Precision and Microsystems Engineering (PME), Delft 2628 CD, The Netherlands;* orcid.org/0000-0001-5799-8527; Email: S.Aghajani@tudelft.nl

Authors

Angelo Accardo − *Delft University of Technology, Faculty of Mechanical, Maritime, and Materials Engineering (3ME), Department of Precision and Microsystems Engineering (PME), Delft 2628 CD, The Netherlands;* orcid.org/0000-0003-0442-3652

Marcel Tichem − *Delft University of Technology, Faculty of Mechanical, Maritime, and Materials Engineering (3ME), Department of Precision and Microsystems Engineering (PME), Delft 2628 CD, The Netherlands*

Complete contact information is available at: https://pubs.acs.org/10.1021/acsanm.0c00887

Notes

The authors declare no competing financial interest.

ACKNOWLEDGMENTS

The authors thank Dr. Ivan Buijnsters for a fruitful discussion about the thermal treatment effect as well as Patrick van Holst, Gideon Emmaneel, Spiridon van Veldhoven, and Rob Luttjeboer for their technical assistance. This project was supported by funding from the Delft University of Technology through the Nano Engineering research Initiative (NERI, www.tudelft.nl/neri).

REFERENCES

(1) Kneipp, K.; Wang, Y.; Kneipp, H.; Perelman, L. T.; Itzkan, I.; Dasari, R. R.; Feld, M. S. Single Molecule Detection Using Surface-Enhanced Raman Scattering (SERS). *Phys. Rev. Lett.* **1997**, *78*, 1667−1670.

(2) Lim, D. K.; Jeon, K. S.; Kim, H. M.; Nam, J. M.; Suh, Y. D. Nanogap-Engineerable Raman-Active Nanodumbbells for Single-Molecule Detection. *Nat. Mater.* **2010**, *9* (1), 60−67.

(3) Kneipp, K.; Kneipp, H.; Kartha, V. B.; Manoharan, R.; Deinum, G.; Itzkan, I.; Dasari, R. R.; Feld, M. S. Detection and Identification of a Single DNA Base Molecule Using Surface-Enhanced Raman Scattering (SERS). *Phys. Rev. E: Stat. Phys., Plasmas, Fluids, Relat. Interdiscip. Top.* **1998**, *57* (6), R6281−R6284.

(4) Kneipp, J.; Kneipp, H.; Kneipp, K. SERS-a Single-Molecule and Nanoscale Tool for Bioanalytics. *Chem. Soc. Rev.* **2008**, *37* (5), 1052−1060.

(5) Ding, S.-Y.; Yi, J.; Li, J.-F.; Ren, B.; Wu, D.-Y.; Panneerselvam, R.; Tian, Z.-Q. Nanostructure-Based Plasmon-Enhanced Raman Spectroscopy for Surface Analysis of Materials. *Nat. Rev. Mater.* **2016**, *1* (6), 16021.

(6) Zheng, J.; He, L. Surface-Enhanced Raman Spectroscopy for the Chemical Analysis of Food. *Compr. Rev. Food Sci. Food Saf.* **2014**, *13* (3), 317−328.

(7) Lane, L. A.; Qian, X.; Nie, S. SERS Nanoparticles in Medicine: From Label-Free Detection to Spectroscopic Tagging. *Chem. Rev.* **2015**, *115* (19), 10489−10529.

(8) Sharma, B.; Frontiera, R. R.; Henry, A. I.; Ringe, E.; Van Duyne, R. P. SERS: Materials, Applications, and the Future. *Mater. Today* **2012**, *15* (1−2), 16−25.

(9) Jensen, L.; Aikens, C. M.; Schatz, G. C. Electronic Structure Methods for Studying Surface-Enhanced Raman Scattering. *Chem. Soc. Rev.* **2008**, *37* (5), 1061.

(10) Willets, K. A.; Van Duyne, R. P. Localized Surface Plasmon Resonance Spectroscopy and Sensing. *Annu. Rev. Phys. Chem.* **2007**, *58* (1), 267−297.

(11) Bell Steven, E. J.; McCourt, M. R. SERS Enhancement by Aggregated Au Colloids: Effect of Particle Size. *Phys. Chem. Chem. Phys.* **2009**, *11* (34), 7348−7349.

(12) Kleinman, S. L.; Frontiera, R. R.; Henry, A. I.; Dieringer, J. A.; Van Duyne, R. P. Creating, Characterizing, and Controlling Chemistry with SERS Hot Spots. *Phys. Chem. Chem. Phys.* **2013**, *15* (1), 21−36.

(13) Hossain, M. K.; Kitahama, Y.; Huang, G. G.; Han, X.; Ozaki, Y. Surface-Enhanced Raman Scattering: Realization of Localized Surface Plasmon Resonance Using Unique Substrates and Methods. *Anal. Bioanal. Chem.* **2009**, *394* (7), 1747−1760.

(14) Liu, M.; Xiang, R.; Lee, Y.; Otsuka, K.; Ho, Y. L.; Inoue, T.; Chiashi, S.; Delaunay, J. J.; Maruyama, S. Fabrication, Characterization, and High Temperature Surface Enhanced Raman Spectroscopic Performance of SiO_2 Coated Silver Particles. *Nanoscale* **2018**, *10* (12), 5449−5456.

(15) Qin, M.; Zhou, X.; Zhu, J.; Ma, M.; Wang, H.; Yang, L. Synthesis of Gold Nanorods with Varied Length-Diameter Ratios-Applications Using SERS for the Detection of Drugs. *J. Dispersion Sci. Technol.* **2019**, 1−8.

(16) Yue, W.; Wang, Z.; Yang, Y.; Chen, L.; Syed, A.; Wong, K.; Wang, X. Electron-Beam Lithography of Gold Nanostructures for Surface-Enhanced Raman Scattering. *J. Micromech. Microeng.* **2012**, *22* (12), 125007.

(17) Li, D.; Liu, J.; Wang, H.; Barrow, C. J.; Yang, W. Electrochemical Synthesis of Fractal Bimetallic Cu/Ag Nanodendrites for Efficient Surface Enhanced Raman Spectroscopy. *Chem. Commun.* **2016**, *52* (73), 10968−10971.

(18) Mao, A.; Ding, M.; Jin, X.; Gu, X.; Cai, C.; Xin, C.; Zhang, T. Direct, Rapid Synthesis of Water-Dispersed Copper Nanoparticles and Their Surface-Enhanced Raman Scattering Properties. *J. Mol. Struct.* **2015**, *1079*, 396−401.

(19) Yuan, Y.-X.; Ling, L.; Wang, X.-Y.; Wang, M.; Gu, R.-A.; Yao, J.-L. Surface Enhanced Raman Spectroscopic Readout on Heavy Metal Ions Based on Surface Self Assembly. *J. Raman Spectrosc.* **2007**, *38* (10), 1280−1287.

(20) He, Y.; Wang, R.; Jiao, T.; Yan, X.; Wang, M.; Zhang, L.; Bai, Z.; Zhang, Q.; Peng, Q. Facile Preparation of Self-Assembled Layered Double Hydroxide-Based Composite Dye Films As New Chemical Gas Sensors. *ACS Sustainable Chem. Eng.* **2019**, *7* (12), 10888−10899.

(21) Wu, W.; Liu, L.; Dai, Z.; Liu, J.; Yang, S.; Zhou, L.; Xiao, X.; Jiang, C.; Roy, V. A. L. Low-Cost, Disposable, Flexible and Highly Reproducible Screen Printed SERS Substrates for the Detection of Various Chemicals. *Sci. Rep.* **2015**, *5* (1), 10208.

(22) Bozzini, B.; D'Urzo, L.; Mele, C. A Novel Polymeric Leveller for the Electrodeposition of Copper from Acidic Sulphate Bath: A Spectroelectrochemical Investigation. *Electrochim. Acta* **2007**, *52* (14), 4767−4777.

(23) Han, R.; Wu, H.; Wan, C.; Pan, W. Templated Nanoporous Copper and Nickel: Novel Substrates for Surface-Enhanced Raman Scattering. *Scr. Mater.* **2008**, *59* (10), 1047−1050.

(24) Diao, F.; Xiao, X.; Luo, B.; Sun, H.; Ding, F.; Ci, L.; Si, P. Two-Step Fabrication of Nanoporous Copper Films with Tunable Morphology for SERS Application. *Appl. Surf. Sci.* **2018**, *427*, 1271−1279.

(25) Lu, Z.; Si, H.; Li, Z.; Yu, J.; Liu, Y.; Feng, D.; Zhang, C.; Yang, W.; Man, B.; Jiang, S. Sensitive, Reproducible, and Stable 3D Plasmonic Hybrids with Bilayer WS 2 as Nanospacer for SERS Analysis. *Opt. Express* **2018**, *26* (17), 21626.

(26) Chan, G. H.; Zhao, J.; Hicks, E. M.; Schatz, G. C.; Van Duyne, R. P. Plasmonic Properties of Copper Nanoparticles Fabricated by Nanosphere Lithography. *Nano Lett.* **2007**, *7* (7), 1947−1952.

(27) Gunnarsson, L.; Bjerneld, E. J.; Xu, H.; Petronis, S.; Kasemo, B.; Käll, M. Interparticle Coupling Effects in Nanofabricated Substrates for Surface-Enhanced Raman Scattering. *Appl. Phys. Lett.* **2001**, *78* (6), 802−804.

(28) Wang, H. N.; Dhawan, A.; Du, Y.; Batchelor, D.; Leonard, D. N.; Misra, V.; Vo-Dinh, T. Molecular Sentinel-on-Chip for SERS-Based Biosensing. *Phys. Chem. Chem. Phys.* **2013**, *15* (16), 6008−6015.

(29) Tabrizi, N. S.; Xu, Q.; van der Pers, N. M.; Schmidt-Ott, A. Generation of Mixed Metallic Nanoparticles from Immiscible Metals by Spark Discharge. *J. Nanopart. Res.* **2010**, *12* (1), 247−259.

(30) Tabrizi, N. S.; Xu, Q.; van der Pers, N. M.; Lafont, U.; Schmidt-Ott, A. Synthesis of Mixed Metallic Nanoparticles by Spark Discharge. *J. Nanopart. Res.* **2009**, *11* (5), 1209−1218.

(31) Reinmann, R.; Akram, M. Temporal Investigation of a Fast Spark Discharge in Chemically Inert Gases. *J. Phys. D: Appl. Phys.* **1997**, *30* (7), 1125−1134.

(32) Tabrizi, N. S.; Ullmann, M.; Vons, V. A.; Lafont, U.; Schmidt-Ott, A. Generation of Nanoparticles by Spark Discharge. *J. Nanopart. Res.* **2009**, *11* (2), 315−332.

(33) Schwyn, S.; Garwin, E.; Schmidt-Ott, A. Aerosol Generation by Spark Discharge. *J. Aerosol Sci.* **1988**, *19* (5), 639−642.

(34) Pfeiffer, T. V.; Feng, J.; Schmidt-Ott, A. New Developments in Spark Production of Nanoparticles. *Adv. Powder Technol.* **2014**, *25* (1), 56−70.

(35) Accardo, A.; Shalabaeva, V.; Cotte, M.; Burghammer, M.; Krahne, R.; Riekel, C.; Dante, S. Amyloid β Peptide Conformational Changes in the Presence of a Lipid Membrane System. *Langmuir* **2014**, *30* (11), 3191−3198.

(36) White, F. M. *Fluid Mechanics*, 7th ed.; McGraw-Hill: 2011.

(37) Buffat, P.; Borel, J. P. Size Effect on the Melting Temperature of Gold Particles. *Phys. Rev. A: At., Mol., Opt. Phys.* **1976**, *13* (6), 2287−2298.

(38) Roduner, E. Size Matters: Why Nanomaterials Are Different. *Chem. Soc. Rev.* **2006**, *35* (7), 583.

(39) Yeshchenko, O. A.; Dmitruk, I. M.; Alexeenko, A. A.; Dmytruk, A. M. Size-Dependent Melting of Spherical Copper Nanoparticles Embedded in a Silica Matrix. *Phys. Rev. B: Condens. Matter Mater. Phys.* **2007**, *75* (8), 085434.

(40) Meng, H.; Chen, Z.; Xing, G.; Yuan, H.; Chen, C.; Zhao, F.; Zhang, C.; Wang, Y.; Zhao, Y. Ultrahigh Reactivity and Grave Nanotoxicity of Copper Nanoparticles. *J. Radioanal. Nucl. Chem.* **2007**, *272* (3), 595−598.

(41) Dhineshbabu, N. R.; Rajendran, V.; Nithyavathy, N.; Vetumperumal, R. Study of Structural and Optical Properties of Cupric Oxide Nanoparticles. *Appl. Nanosci.* **2016**, *6* (6), 933−939.

(42) Hornés, A.; Hungría, A. B.; Bera, P.; López Cámara, A.; Fernández-García, M.; Martínez-Arias, A.; Barrio, L.; Estrella, M.; Zhou, G.; Fonseca, J. J.; Hanson, J. C.; Rodriguez, J. A. Inverse CeO_2/CuO Catalyst as an Alternative to Classical Direct Configurations for Preferential Oxidation of CO in Hydrogen-Rich Stream. *J. Am. Chem. Soc.* **2010**, *132* (1), 34−35.

(43) Teixeira, C. D. O. P.; Montani, S. D. S.; Palacio, L. A.; Zotin, F. M. Z. The Effect of Preparation Methods on the Thermal and Chemical Reducibility of Cu in Cu-Al Oxides. *Dalt. Trans.* **2018**, *47* (32), 10989−11001.

(44) Kirsch, P. D.; Ekerdt, J. G. Chemical and Thermal Reduction of Thin Films of Copper (II) Oxide and Copper (I) Oxide. *J. Appl. Phys.* **2001**, *90* (8), 4256−4264.

(45) Pike, J.; Chan, S.-W.; Zhang, F.; Wang, X.; Hanson, J. Formation of Stable Cu_2O from Reduction of CuO Nanoparticles. *Appl. Catal., A* **2006**, *303* (2), 273−277.

(46) Müller, H. Optical Properties of Metal Clusters. *Z. Phys. Chem.* **1996**, *194*, 278.

(47) Hartland, G. V. Optical Studies of Dynamics in Noble Metal Nanostructures. *Chem. Rev.* **2011**, *111* (6), 3858−3887.

(48) Link, S.; El-Sayed, M. A. Spectral Properties and Relaxation Dynamics of Surface Plasmon Electronic Oscillations in Gold and Silver Nanodots and Nanorods. *J. Phys. Chem. B* **1999**, *103* (40), 8410−8426.

(49) Scholl, J. A.; Koh, A. L.; Dionne, J. A. Quantum Plasmon Resonances of Individual Metallic Nanoparticles. *Nature* **2012**, *483* (7390), 421−427.

(50) Yeshchenko, O. A.; Dmitruk, I. M.; Dmytruk, A. M.; Alexeenko, A. A. Influence of Annealing Conditions on Size and Optical Properties of Copper Nanoparticles Embedded in Silica Matrix. *Mater. Sci. Eng., B* **2007**, *137* (1−3), 247−254.

(51) Zhang, M.-L.; Fan, X.; Zhou, H.-W.; Shao, M.-W.; Zapien, J. A.; Wong, N.-B.; Lee, S.-T. A High-Efficiency Surface-Enhanced Raman Scattering Substrate Based on Silicon Nanowires Array Decorated with Silver Nanoparticles. *J. Phys. Chem. C* **2010**, *114* (5), 1969−1975.

(52) Pereira, A. J.; Gomes, J. P.; Lenz, G. F.; Schneider, R.; Chaker, J. A.; De Souza, P. E. N.; Felix, J. F. Facile Shape-Controlled Fabrication of Copper Nanostructures on Borophosphate Glasses: Synthesis, Characterization, and Their Highly Sensitive Surface-Enhanced Raman Scattering (SERS) Properties. *J. Phys. Chem. C* **2016**, *120* (22), 12265−12272.

(53) Li, C.; Yu, J.; Xu, S.; Jiang, S.; Xiu, X.; Chen, C.; Liu, A.; Wu, T.; Man, B.; Zhang, C. Constructing 3D and Flexible Plasmonic Structure for High-Performance SERS Application. *Adv. Mater. Technol.* **2018**, *3* (11), 1−11.

(54) Suresh, V.; Ding, L.; Chew, A. B.; Yap, F. L. Fabrication of Large-Area Flexible SERS Substrates by Nanoimprint Lithography. *ACS Appl. Nano Mater.* **2018**, *1* (2), 886−893.

(55) El-Aal, M. A.; Seto, T.; Kumita, M.; Abdelaziz, A. A.; Otani, Y. Synthesis of Silver Nanoparticles Film by Spark Discharge Deposition for Surface-Enhanced Raman Scattering. *Opt. Mater. (Amsterdam, Neth.)* **2018**, *83* (April), 263−271.

(56) Fu, P.; Shi, X.; Jiang, F.; Xu, X. Superhydrophobic Nanostructured Copper Substrate as Sensitive SERS Platform Prepared by Femtosecond Laser Pulses. *Appl. Surf. Sci.* **2020**, *501*, 144269.

(57) Chen, L. Y.; Yu, J. S.; Fujita, T.; Chen, M. W. Nanoporous Copper with Tunable Nanoporosity for SERS Applications. *Adv. Funct. Mater.* **2009**, *19* (8), 1221−1226.

(58) Xu, S.; Tang, W.; Chase, D. B.; Sparks, D. L.; Rabolt, J. F. A Highly Sensitive, Selective, and Reproducible SERS Sensor for Detection of Trace Metalloids in the Environment. *ACS Appl. Nano Mater.* **2018**, *1* (3), 1257−1264.

(59) Suresh, V.; Ding, L.; Chew, A. B.; Yap, F. L. Fabrication of Large-Area Flexible SERS Substrates by Nanoimprint Lithography. *ACS Appl. Nano Mater.* **2018**, *1* (2), 886−893.

(60) Zhang, X.; Mo, Y.; Liu, B.; Hu, C.; Chen, S.; Shi, H.; Chen, J. Fabrication of Scale-like Silver-Nanosheets-Grafted Carbon-Fenced Conductive Silver Nanowires as E Ff Ective 3D SERS Substrates. *ACS Appl. Nano Mater.* **2018**, *1*, 4771.

(61) Accardo, A.; Courson, R.; Riesco, R.; Raimbault, V.; Malaquin, L. Direct Laser Fabrication of Meso-Scale 2D and 3D Architectures with Micrometric Feature Resolution. *Addit. Manuf.* **2018**, *22*, 440−446.

(62) Kramer, R. C. L. N.; Verlinden, E. J.; Angeloni, L.; Van Den Heuvel, A.; Fratila-Apachitei, L. E.; Van Der Maarel, S. M.; Ghatkesar, M. K. Multiscale 3D-Printing of Microfluidic AFM Cantilevers. *Lab Chip* **2020**, *20* (2), 311−319.